

# Slip-activated surface creep with room-temperature super-elongation in metallic nanocrystals

Li Zhong<sup>1</sup>, Frederic Sansoz<sup>2\*</sup>, Yang He<sup>1</sup>, Chongmin Wang<sup>3</sup>, Ze Zhang<sup>4</sup> and Scott X. Mao<sup>1\*</sup>

**Nanoscale metallic crystals have been shown to follow a ‘smaller is stronger’ trend. However, they usually suffer from low ductility due to premature plastic instability by source-limited crystal slip. Here, by performing *in situ* atomic-scale transmission electron microscopy, we report unusual room-temperature super-elongation without softening in face-centred-cubic silver nanocrystals, where crystal slip serves as a stimulus to surface diffusional creep. This interplay mechanism is shown experimentally and theoretically to govern the plastic deformation of nanocrystals over a material-dependent sample diameter range between the lower and upper limits for nanocrystal stability by surface diffusional creep and dislocation plasticity, respectively, which extends far beyond the maximum size for pure diffusion-mediated deformation (for example, Coble-type creep). This work provides insight into the atomic-scale coupled diffusive-displacive deformation mechanisms, maximizing ductility and strength simultaneously in nanoscale materials.**

Crystal slip by dislocation emission or twinning<sup>1,2</sup>, and atom diffusion along surfaces and interfaces<sup>3–6</sup> are generally viewed as two major competing modes of plastic deformation in nanoscale materials<sup>7–12</sup>. The limited source and interaction of crystal dislocations in small-volume and nanocrystalline materials give rise to superior strengths with reduced ductility<sup>2,11,13–21</sup>. In contrast, surface- or interface-assisted defect diffusion enhances creep rates at the atomic scale, thereby leading to strain softening without premature failure<sup>3,10,11</sup>. This dichotomy is particularly evident in metals as the size decreases to the nanoscale. An extreme example has recently been observed in sub-10-nm Ag nanoparticles showing surface-diffusion-mediated liquid-like behaviour even at room temperature<sup>22</sup>, while conversely Ag nanowires (NWs) above 40 nm in diameter have been found to undergo dislocation-dominated plasticity with diameter-dependent strength following the classical ‘smaller is stronger’ power-law scaling<sup>23</sup>. A recent experimental study on the temperature dependence of strength in pristine Pd NWs<sup>21</sup>, however, suggested a potential relationship between dislocation nucleation and surface diffusion at small scale. Given the important roles that surfaces and interfaces play for both dislocation nucleation<sup>24,25</sup> and diffusional creep<sup>22</sup> in nanocrystals, these observations raise the possibility that coupled diffusive-displacive processes may replace pure crystal slip or diffusional creep, and govern the plastic deformation of nanocrystals within a critical size regime<sup>7,8,26,27</sup>. Unfortunately, the atomistic diffusive process in this crossover regime has never been directly observed.

Here, we performed *in situ* transmission electron microscopy (TEM), complemented by molecular dynamics (MD) simulations and kinetics theory, to study deformation mechanisms in sub-100-nm-sized Ag and Pt nanocrystals made with fresh surfaces<sup>28,29</sup> (see Methods and Supplementary Figs 1 and 2 for details). We find direct experimental and theoretical evidence for an unusual room-temperature superplastic behaviour at elevated strength in

Ag nanocrystals with diameters between 15 nm and 80 nm, which is considered to be well above the maximum size where surface-assisted Coble-type creep is expected to dominate plasticity<sup>22</sup>. This phenomenon arises from a slip-activated surface creep mechanism where atomic-scale surface-step diffusion, activated by surface dislocation nucleation events, is effective in eliminating the tendency for plastic instability and localized necking that limit the ductility, and thus has significant implications for developing advanced nanodevices with ultrahigh strength and deformability.

Figure 1 presents two representative *in situ* TEM experiments demonstrating profound differences in mechanical behaviour between single-crystalline Ag and Pt nanocrystals at room temperature. Under  $\langle 112 \rangle$  tensile loading at a strain rate of  $\sim 10^{-3} \text{ s}^{-1}$ , a 59-nm-diameter Ag nanocrystal exhibited an unprecedented amount of plastic deformation (Fig. 1a–c) carried by the continuous flow of surface steps (Fig. 1d) and partial dislocations (indicated by orange arrows in Fig. 1b and its inset), reaching a uniform elongation of  $\sim 90\%$  before the onset of necking (Fig. 1c). Such superplastic behaviour (up to 200% uniform elongation) was observed in Ag nanocrystals with diameters in the range 15–80 nm under different loading directions (Supplementary Fig. 3 and Supplementary Movies 1 and 2), which is not expected in the dislocation-mediated deformation of nanocrystals that is often associated with poor resistance to plastic instability<sup>21</sup>, even if geometrical effects from the small aspect ratio of the Ag junction could enhance ductility<sup>30</sup>. In stark contrast, limited ductility (Fig. 1e–g and Supplementary Movie 3) and even rigid-shear-like behaviour (Supplementary Fig. 4) were observed in Pt nanocrystals deformed at equivalent strain rates. In Pt, plastic instability by shear localization from crystal slip was manifest at an early stage of deformation (Fig. 1f), followed by rapid formation of a narrow neck (Fig. 1g). By measuring the normalized pre-necking elongation ( $\epsilon_N$ ) of as-formed Ag and Pt nanocrystals with

<sup>1</sup>Department of Mechanical Engineering and Materials Science, University of Pittsburgh, Pittsburgh, Pennsylvania 15261, USA. <sup>2</sup>Department of Mechanical Engineering and Materials Science Program, The University of Vermont, Burlington, Vermont 05405, USA. <sup>3</sup>Environmental Molecular Sciences Laboratory, Pacific Northwest National Laboratory, Richland, Washington 99352, USA. <sup>4</sup>Department of Materials Science and Engineering and State Key Laboratory of Silicon Materials, Zhejiang University, Hangzhou 310027, China. \*e-mail: frederic.sansoz@uvm.edu; sxm2@pitt.edu

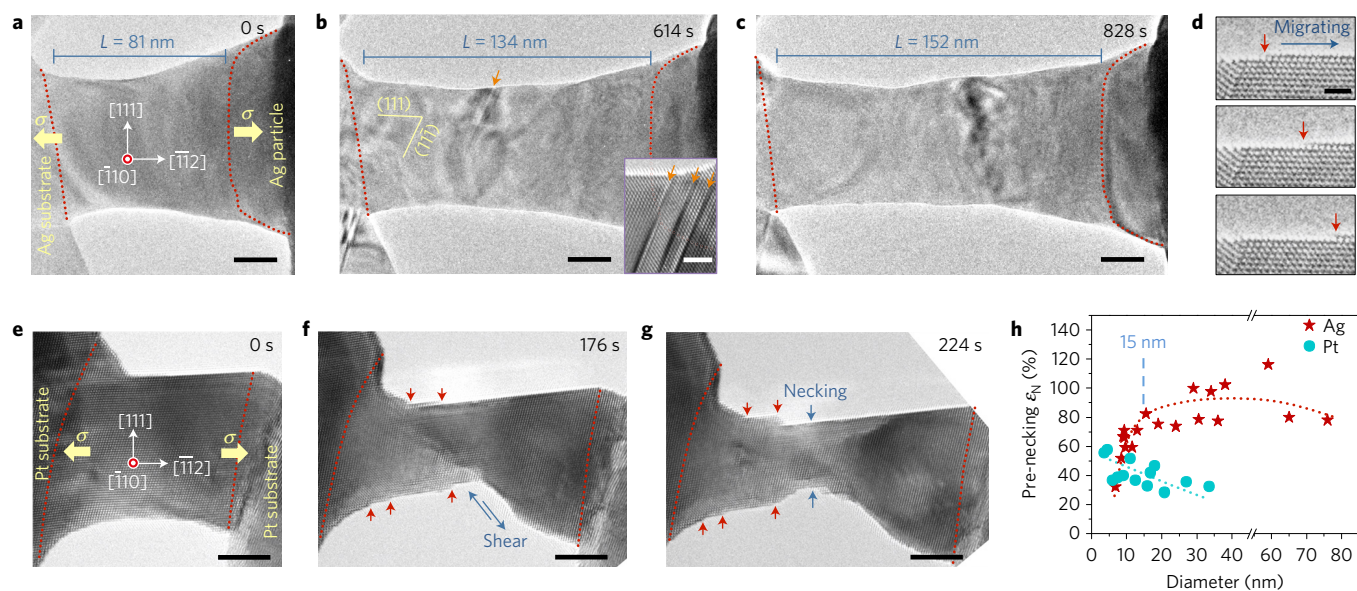


**Figure 1 | Fundamental difference in room-temperature mechanical behaviours between single-crystalline Ag and Pt nanocrystals observed by *in situ* TEM.** **a–c**, Ultra-large plasticity in a 59-nm-diameter Ag nanocrystal under  $\langle 112 \rangle$  tensile loading at a strain rate of  $\sim 10^{-3} \text{ s}^{-1}$ . A uniform elongation of 90% of the gauge section (outlined by red dotted curves) was reached before the onset of necking. The nanocrystal was formed by welding a Ag nanoparticle deposited on a tungsten probe to a Ag nano-tip protruding from a substrate through a melt-quenching process (see Methods). Stacking faults (SF) formed by the emission of Shockley partial dislocations were frequently observed throughout the deformation process, as indicated by orange arrow heads in **b** and its inset. **d**, Close-up view on the continuous lateral movement of surface steps along the (111) surface plane during tensile straining (tracked by red arrow heads). **e–g**, Shear localization (**f**) and necking (**g**) observed at an early stage of deformation of a  $\langle 112 \rangle$ -oriented 14-nm-diameter Pt nanocrystal formed by welding two Pt nano-tips together (see Methods). The gauge section is indicated by red dotted curves. The strain rate was controlled to be  $\sim 2 \times 10^{-3} \text{ s}^{-1}$ . Note that surface steps formed by crystal slip in Pt nanocrystals remained immobile (marked by red arrow heads). **h**, Normalized elongation before necking as a function of diameter in single-crystalline Ag and Pt nanocrystals. The measured elongation is normalized by  $D/L$ , with  $D$  and  $L$  the diameter and length of the nanocrystals before deformation, respectively. The applied strain rates were on the order of  $10^{-3} \text{ s}^{-1}$ . Scale bars are 20 nm (**a–c**), 2 nm (inset in **b**), 1 nm (**d**), and 5 nm (**e–g**).

different diameters and lengths (Supplementary Section 1 and Supplementary Fig. 5), Fig. 1h shows that uniform ductility in Ag nanocrystals is overwhelmingly superior to that in Pt nanocrystals, except in sub-15-nm nanocrystals, where the former is found to reduce sharply with decreasing diameter. These results are surprising because bulk Ag and Pt single-crystalline metals are known to exhibit similarly high intrinsic ductilities<sup>31</sup>. Interestingly, the migration of surface steps was not observed in the deformed Pt nanocrystals (Fig. 1f,g and Supplementary Fig. 4). This difference is consistent with a twofold to threefold increase in the activation energy barrier for atomic surface diffusion in Pt compared to Ag<sup>32,33</sup>, suggesting that surface atom diffusion plays an important role.

Atomically resolved dislocation dynamics was captured during tensile loading of a 20-nm-diameter Ag nanocrystal that exhibited superplastic response at room temperature (Fig. 1h). Figure 2a shows the emission of one dislocation (indicated by a yellow arrow head) from a surface source (circled in cyan), forming an atomic-scale step at the free surface (marked by a purple arrow). The as-formed surface step instantly moved on the (111) sidewall towards the bulk substrate in the right-hand side of the image (Fig. 2b,c and Supplementary Movie 4). With subsequent straining, more surface steps (Fig. 2d,e) emerged from the stressed region of smaller diameter, and migrated towards the thicker region. Such surface ledge motion occurred at an average velocity of 0.2 to 1 nm  $\text{s}^{-1}$  without interruption (Supplementary Fig. 6 and Supplementary Movie 4), which cannot be explained by the discrete dislocation plasticity expected at such a small scale<sup>25</sup>. Rather, continuous ledge flow was attributed to surface diffusion mediated by dislocation plasticity, since two of the three surface steps in Fig. 2 were directly seen to nucleate and migrate after the emission of new surface dislocations (Fig. 2a,e). Given the low electron beam

intensity applied during observation ( $< 10^5 \text{ A m}^{-2}$ ), the temperature rise induced by beam irradiation was negligible<sup>22,34</sup>. However, the small activation energy for single-atom diffusion on low-indexed Ag surfaces<sup>32,33</sup> supports the hypothesis that lateral movements of surface ledges arise from curvature- and stress-driven diffusional creep<sup>8,22</sup> by sequential hopping of atoms present on the surface step<sup>35</sup>, as schematically depicted in Fig. 2f.

Despite technological difficulties associated with capturing short-lived dislocation dynamics in nanocrystals<sup>20,36</sup>, for example the lack of crystal slip accompanying the nucleation of Step 2 in Fig. 2d, our *in situ* TEM made it possible to reveal a special interplay between surface diffusion and dislocation plasticity in the superplastic size regime of Ag nanocrystals. Specifically, individual slip events were systematically examined in Fig. 3 by quantitatively monitoring the separation distance between two (111) reference planes across a perfect single crystal during straining. Each surface-step nucleation event (Fig. 3b,d), which served as the onset of the surface ledge flow (for example, Fig. 3c), was found to coincide with an abrupt elongation ( $\Delta L$ ) of slightly less than 0.2 nm, in good agreement with the projection of a  $(1/2)[110]$  slip on the  $[112]$  loading direction. Tracking the nucleation and motion of fifteen surface steps separately allowed us to conclude that surface diffusion becomes active only after dislocation emission in Ag nanocrystals with diameters above 15 nm, revealing a slip-activated surface creep mechanism.

Such a deformation mechanism not only leads to ultrahigh uniform plasticity, but also ensures that surface ledge diffusion proceeds at very high stresses near the yield point of the nanocrystal (Supplementary Fig. 7), therefore exempting plastic softening associated with a pure diffusion-mediated creep mechanism<sup>10,12,37</sup>. To better support this conclusion, we performed MD simulations with  $\langle 112 \rangle$ -oriented NWs consisting of a double conical shape

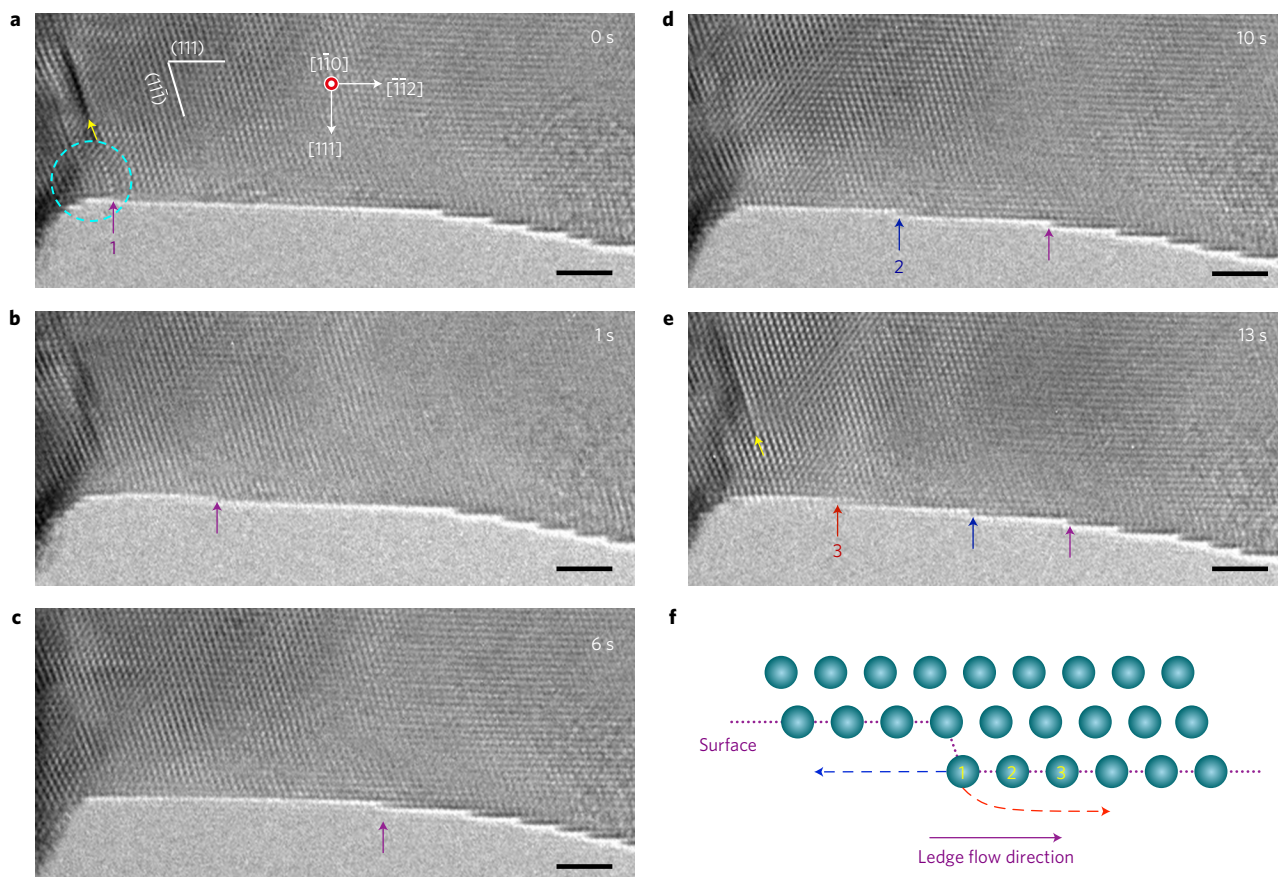


**Figure 2 | Surface diffusive plasticity during tensile deformation of a 20-nm Ag nanocrystal. a–e**, Surface-diffusion-assisted migration of three atomic steps on the {111} sidewall of the nanocrystal. Dislocations (marked by yellow arrows in **a** and **e**) were emitted from the corner circled in cyan colour, forming surface steps that quickly moved away from the highly stressed region. Each surface step is tracked by an arrow of specific colour. **f**, Schematics of surface migration by sequential hopping of atoms from the step edge. An atom at the surface step (Atom 1) has fewer neighbouring atoms and thus a higher chemical potential compared to the other surface atoms, which drives Atom 1 to migrate towards surface sites with lower chemical potentials (indicated by red and blue dash arrows). This process is repeated to the next atom on the surface step (for example, Atoms 2 and 3), resulting in continuous lateral movement of the step. All scale bars are 2 nm.

(see Methods for details), and have obtained MD-based strength estimates for NWs deformed at our experimental strain rates,  $\sim 0.007 \text{ s}^{-1}$  (Supplementary Section 2 and Supplementary Fig. 8 and Supplementary Table 1). A tensile yield strength in a 20-nm-diameter Ag NW (similar in size to that in Fig. 2) was found to be on the order of 2.97 GPa. Using the Young's modulus of Ag for the  $\langle 112 \rangle$  crystal direction (Supplementary Table 1), the corresponding elastic strain limit at room temperature was estimated to be 3.5%. Apparently, the  $\sim 3.4\%$  strain limit measured directly from *in situ* TEM lattice strain (Supplementary Fig. 7) proves that nanocrystals have experimentally maintained high stresses that are close to the ideal MD-based estimates.

From an atomistic perspective, emission of a dislocation generates an atomic step that leads to an abrupt change in surface contour with a local difference in chemical potential  $\mu$  (Fig. 3e middle). Due to curvature- and stress-driven rapid surface diffusion of Ag atoms at the step edge (Fig. 2f), the as-formed surface step migrates to a position where the overall smooth and uniform surface contour with low chemical potential before the slip event is recovered (Fig. 3e right; schematically illustrated by the red contour in Supplementary Fig. 9). This process, as directly observed in Fig. 2a–e, Fig. 3a–d, and Supplementary Movie 4, therefore gives rise to a self-healing mechanism during plastic deformation that spatially redistributes surface-dislocation-nucleation-controlled crystal slips over the gauge length, thus eliminating the tendency for plastic instability (Fig. 1a–c and Supplementary Figs 2 and 3,

and Supplementary Movies 1 and 2). In contrast, owing to the lack of surface atom diffusion, and consequently surface healing in Pt nanocrystals, crystal slips generate immobile surface steps that induce unrecoverable surface stress concentrations, which serve as a primary source for subsequent surface dislocation emissions. Further crystal slips increase the height of the as-formed surface steps (Supplementary Fig. 10), and eventually lead to localized shear and premature necking (Fig. 1f,g and Supplementary Fig. 4b,c,e and Supplementary Movie 3; schematically illustrated by the blue contour in Supplementary Fig. 9).

The impact of slip-activated surface creep on the mechanical behaviour of metallic nanocrystals is further reflected in a negative dependence of ductility on strain rate in Ag nanocrystals (Fig. 4a), which is opposite to the strain-rate dependence previously reported in bicrystalline Ag nanowires with surface diffusion suppressed by a surface contamination layer formed during electron-beam-assisted Pt deposition<sup>38</sup>. We hypothesized that the sharp decrease in ductility at strain rates above  $\sim 0.02 \text{ s}^{-1}$  corresponds to the regime where the relatively slow surface diffusional creep (on a timescale of seconds as shown in Supplementary Fig. 6) can no longer keep up with dislocation plasticity, leading to localized crystal slips and sharp surface contour changes (Supplementary Fig. 11) that are, to some extent, similar to those in Pt nanocrystals. The ductility of Ag nanocrystals in this high-strain-rate regime (Fig. 4a) is found to be on par with that of Pt nanocrystals under slip-dominated plastic deformation (Fig. 1h).

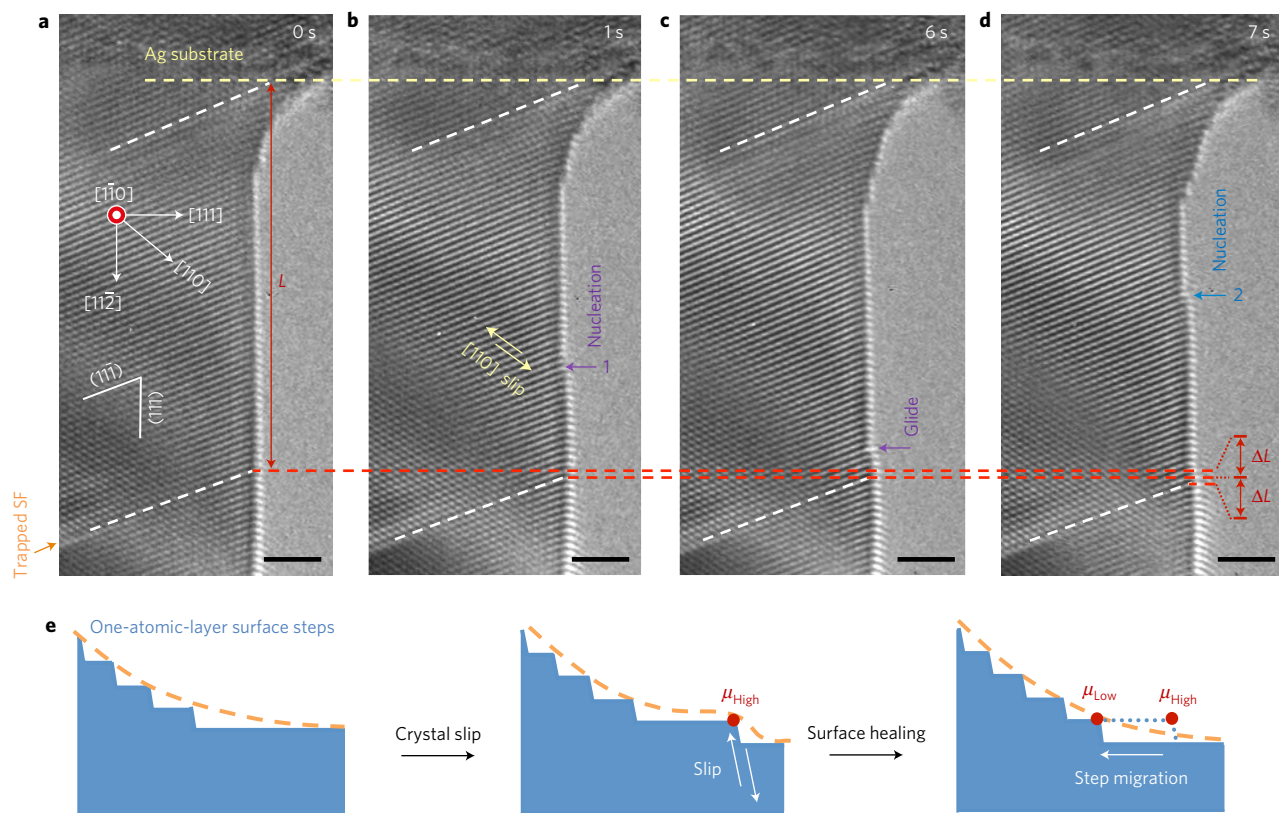


**Figure 3 | Slip-activated surface diffusional creep in Ag nanocrystals.** **a**, High-resolution TEM image of a pristine Ag nanocrystal under  $(11\bar{2})$  tensile loading. Crystal slips are identified by monitoring the change in length  $L$  between two reference  $(11\bar{1})$  planes marked by white dashed lines. The boundary between the nanocrystal and substrate (yellow dash line) and a trapped stacking fault (orange arrow head) were used for the position of the two reference planes. **b**, Nucleation of a surface step (purple arrow) accompanied by a sudden elongation of  $\Delta L$ , which matches a  $(1/2)[110]$  slip on either the  $(\bar{1}11)$  or  $(1\bar{1}1)$  plane projected on the  $[11\bar{2}]$  loading direction, indicating that the step was formed by emission of one dislocation. Note that the slip proceeded on an inclined slip plane, and thus the associated lattice dislocation cannot be observed along the current viewing direction. **c**, Glide of the as-formed surface step, resulting in no sudden changes in  $L$ . **d**, Nucleation of a second surface step (blue arrow) that leads to another abrupt elongation of  $\Delta L$ , proving that the observed surface diffusive plasticity is activated by crystal slip. All scale bars are 2 nm. **e**, Schematic illustration of slip-activated surface creep and associated self-healing mechanism to maintain an overall smooth and uniform surface contour with low chemical potential. Orange dash curves outline the surface contour of the nanocrystal.

A ten orders of magnitude difference exists between simulation and experimental strain rates, making direct comparison of deformation mechanisms difficult, especially when diffusion is involved. By varying the temperature (300–900 K) and strain rate ( $4 \times 10^7 \text{ s}^{-1}$  –  $4 \times 10^8 \text{ s}^{-1}$ ), however, our MD simulations (Fig. 4b; see Methods for details) also demonstrated a direct link between surface atom diffusion and the negative strain-rate dependence of ductility accompanying the superplastic behaviour of Ag NWs. For both Ag and Pt under all conditions, crystal slip always initiated in the narrowest section of the NW, and atom diffusion, if any, remained confined at the surface within one to two atomic layers (Supplementary Figs 12 and 13, respectively). Plastic deformation after yielding continued by forming abundant stacking faults and deformation twinning on the  $\{111\}$  slip planes for the two metals until necking (Supplementary Fig. 14). Remarkably, Fig. 4c and Supplementary Fig. 15a,b show a dramatic increase in pre-necking elongation from 25% to 126% strain in Ag NWs deformed at a strain rate of  $4 \times 10^7 \text{ s}^{-1}$  when the temperature increased from 300 K to 900 K, which corresponds to an increase of homologous temperature from  $0.24T_m$  to  $0.72T_m$ , respectively, with  $T_m = 1,250 \text{ K}$  the melting temperature for Ag. Such superplastic behaviour in Ag NWs at high temperature and a strain rate of  $4 \times 10^7 \text{ s}^{-1}$  coincided with significant atom diffusion on pre-existing surface steps that maintained a relatively smoother surface contour until necking (Fig. 4d and Supplementary

Fig. 14c and Supplementary Movie 5). In contrast, at a strain rate of  $4 \times 10^8 \text{ s}^{-1}$  and all temperatures tested, Fig. 4c shows that Ag NWs exhibited identical lower ductilities (44–46%) associated with limited surface diffusion and slip-induced stepped contours (Fig. 4e and Supplementary Fig. 14b and Supplementary Movie 6), leading to early localized shearing (Supplementary Fig. 14a). As a result, the strain-rate dependence of ductility in Ag NWs predicted by MD (Fig. 4c) changed from positive at 300 K, in agreement with the experimentally observed brittle-to-ductile transition in Ag NWs deformed with increasing strain rates under slip-dominated plasticity<sup>38</sup>, to moderately or strongly negative at 600 K and 900 K when progressively more surface diffusional creep was involved, consistent with the negative dependence observed experimentally in Fig. 4a. At the same absolute temperatures, the smaller homologous temperatures and higher surface atom diffusion barrier of Pt compared to those of Ag lead to negligible surface diffusion in the former (Supplementary Fig. 13), as was the case in our experiments, resulting in limited uniform elongation ( $<35\%$ ) (Supplementary Fig. 15c,d) and its positive dependence on strain rate (Fig. 4c) with localized shear failure under all temperature and strain rate conditions (Supplementary Fig. 14d,e). In summary, our Ag and Pt simulations provided direct computational evidence that the unusual negative dependence of ductility on strain rate in Ag nanocrystals under surface-dislocation-nucleation-controlled plastic deformation emerges only with enhanced surface diffusional

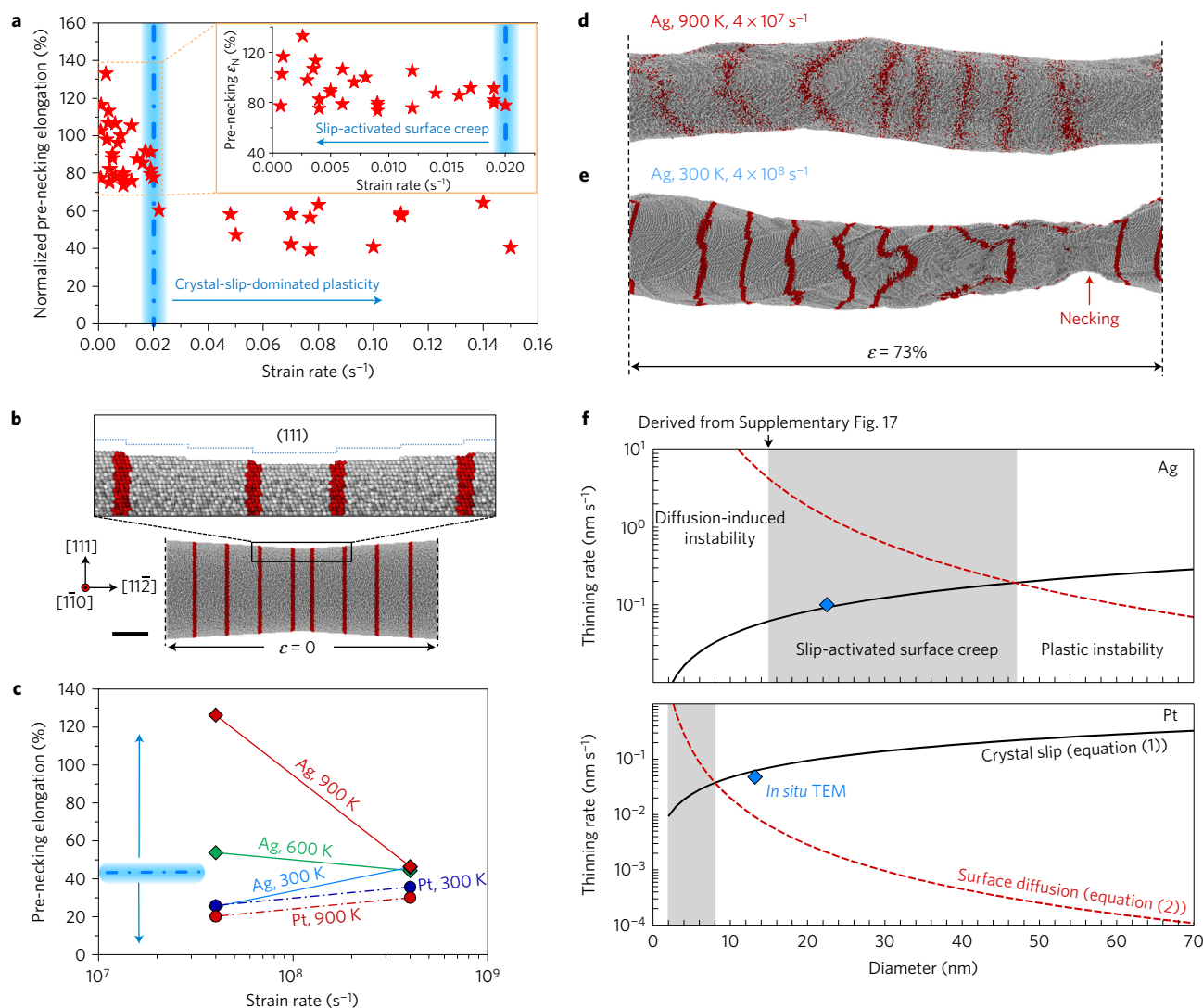


**Figure 4 | Strain-rate and diameter dependences of tensile ductility driven by crystal slip and surface atom diffusion in  $\langle 112 \rangle$ -oriented Ag and Pt nanowires subjected to uniaxial deformation at a constant strain rate.** **a**, Normalized pre-necking elongation as a function of strain rate during tensile straining of  $\langle 112 \rangle$ -oriented Ag nanocrystals with diameters varying between 20–50 nm in experiments. The inset is a close-up view of the low-strain-rate regime below  $0.02 \text{ s}^{-1}$  where super-elongation originates from slip-activated surface diffusional creep. When strain rate exceeds  $\sim 0.02 \text{ s}^{-1}$ , surface diffusional creep can no longer keep up with dislocation plasticity, leading to a sharp decrease in the ductility. **b**, Atomistic model of a  $\langle 112 \rangle$  Ag NW with double conical shape and non-uniform surface morphology associated with  $\{111\}$  terraces and surface steps. Red vertical markers have been added to highlight the initial position of atoms present on several surface steps. The scale bar is 10 nm. **c**, Strain-rate dependence of pre-necking elongation predicted by MD simulations at different temperatures using the atomistic model in **b**. Two different regimes of plasticity with either positive or negative strain-rate dependence of ductility are delineated using downward and upward vertical arrows, respectively. **d,e**, MD snapshots of plastic deformation of Ag NWs up to 73% strain at different temperatures and engineering strain rates: 900 K,  $4 \times 10^7 \text{ s}^{-1}$  (**d**) and 300 K,  $4 \times 10^8 \text{ s}^{-1}$  (**e**). Superplasticity with uniform elongation was accompanied by surface diffusion (red coloured atoms) at 900 K and a strain rate of  $4 \times 10^7 \text{ s}^{-1}$ , while plastic instability with negligible diffusion led to premature necking and NW failure at 300 K and a strain rate of  $4 \times 10^8 \text{ s}^{-1}$ . **f**, Calculations of thinning rates in plastically strained metallic nanocrystals based on crystal slip theory (solid lines) and strain-dependent surface diffusion theory (dashed lines), as a function of nanocrystal diameter. Slip-activated surface creep (shaded area) is operative for diameters between the diffusion stability limit established by spontaneous tip-blunting experiments (Supplementary Fig. 17) and the plastic stability regime where diffusion thinning rates are equal to, or larger than, crystal slip thinning rates. Blue diamonds represent the thinning rates directly measured from *in situ* TEM experiments.

creep, which in our experiments was produced by the slip-activated surface diffusion mechanism (Fig. 3).

Preventing shear localization via slip-activated surface creep thus requires that the crystal thinning rate arising from surface atom diffusion be at least comparable to that based on surface dislocation nucleation. Since crystal slip and surface diffusion rates depend on diameter, shape and type of metals, we have developed a theory predicting the thinning rate based on these two mechanisms under the current experimental configuration,

to estimate the plastic stability limit that outlines the maximum size for slip-activated surface creep (Supplementary Section 3 and Supplementary Table 2 and Supplementary Fig. 16). The thinning rate from crystal slip was expressed as a function of applied strain rate and the initial aspect ratio of the nanocrystal,  $L/D$ , such as

$$\frac{\Delta D}{\Delta t} = \frac{L \sin \alpha}{\cos \alpha - (\varepsilon_0 L/D) \sin \alpha} \dot{\varepsilon} \quad (1)$$

where  $\alpha$  is the projected angle of slip with respect to the tensile loading direction and  $\varepsilon_0$  is the elastic strain limit. Meanwhile, the thinning rate based on curvature- and stress-driven surface diffusion was found equal to

$$\frac{\Delta D}{\Delta t} = \frac{8\delta_s\mu_s}{L^2\rho} \left[ \frac{2\gamma}{D} + \frac{15E\varepsilon_0^2}{32} \right] \quad (2)$$

where  $\delta_s$  is the thickness of drifting surface atoms,  $\mu_s$  is the surface mobility,  $\rho$  is the density,  $\gamma$  is the surface energy, and  $E$  is the Young's modulus. With the surface diffusivities of nanocrystals derived experimentally from the spontaneous tip-blunting rates (Supplementary Section 4 and Supplementary Table 2) and average strain rates of  $0.007\text{ s}^{-1}$  and  $0.008\text{ s}^{-1}$  for Ag and Pt, respectively, in our *in situ* TEM experiments, the proposed theory enables a direct comparison of thinning rates in Ag and Pt nanocrystals as a function of diameter, as shown in Fig. 4f. Under an aspect ratio  $L/D = 1$ , the plastic stability limit, when thinning rates by surface diffusion and crystal slip are equal, is predicted to be 47 nm in Ag nanocrystals, while it decreases dramatically to only 8 nm for Pt nanocrystals. In addition, the *in situ* TEM thinning rates derived from Ag and Pt nanocrystals with  $L/D \sim 1$  (blue diamonds) agreed well with the crystal slip theory (solid lines), corroborating crystal slip as the rate-controlling process in both metals. However, the diameters of Ag and Pt nanocrystals are situated within and outside the plastic stability limit, respectively, which rationalizes the dramatic differences between their mechanical behaviours (Fig. 1). For all aspect ratios of nanocrystals tested by *in situ* TEM (Supplementary Fig. 5), our theory predicts upper bounds for slip-activated surface creep varying in the ranges 36 nm–102 nm and 4 nm–14 nm for Ag and Pt nanocrystals, respectively, matching well with the experimental results presented in Fig. 1h.

Even though we have shown that the onset of surface creep relies on crystal slip (that is, the nucleation of surface steps) in the superplastic size regime (Figs 2 and 3), it is conceivable that when the crystal size drops below a critical diameter (that is, the diffusion stability limit), the driving force induced by curvature is sufficient to break the shape of nanocrystals by surface diffusion without crystal slip, thereby demarcating the lower bound of diameters for slip-activated surface creep. The diffusion stability limits for Pt and Ag nanocrystals were derived in this study from *in situ* TEM analysis of radius stability during spontaneous tip blunting of tapered metallic NWs (Supplementary Fig. 17), and were estimated to be 2 nm and 15 nm, respectively, in good agreement with the overwhelmingly larger thinning rates by diffusion compared to those via crystal slip below these critical diameters (Fig. 4f). In addition, the latter has also been corroborated by experimental observation of surface-diffusion-mediated liquid-like behaviour<sup>22</sup> in sub-15-nm-sized Ag nanocrystals (Supplementary Fig. 18 and Supplementary Movie 7), which led to softening (Supplementary Fig. 7) and a rapid reduction in ductility (Fig. 1h).

This work reveals a slip-activated surface creep mechanism operating within a critical size regime bounded by the lower and upper limits for nanocrystal stability via surface diffusional creep and dislocation plasticity, respectively, which could be applicable to other types of interface-dominated metallic nanostructures, such as nanocrystalline metals. Given that grain boundaries and nanocrystal surfaces both play important roles in dislocation-mediated plasticity and atom diffusion, the mechanism reported here may be relevant to similar interplays between intragranular crystal slip and grain-boundary-mediated diffusive processes<sup>27</sup>, especially in metals with relatively low interface diffusion energy barriers. Nevertheless, such an interplay between dislocation slip and surface diffusion has not yet been reported, due to experimental difficulties in tracking dislocation dynamics at high speed, as well as to the short accessible timescale (generally in the nanoseconds) in

MD simulations, which allows only limited diffusion. In addition, surface diffusion is sensitive to surface contamination (for example, oxidation layers, contamination layers formed by focused ion beam milling and electron/ion beam-assisted Pt deposition, and surfactant layers formed after chemical synthesis), and is thus very likely suppressed in most previous *in situ* studies on the deformation of nanocrystals<sup>23,38–45</sup>. By fabricating nanocrystals with fresh surfaces, we have presented a dynamic picture of room-temperature surface creep activated by dislocation nucleation, which imparts ultrahigh plasticity without compromising the strength, and could set a new paradigm for understanding size-dependent ductility among different nanoscale metals.

## Methods

Methods and any associated references are available in the [online version of the paper](#).

Received 22 June 2016; accepted 28 October 2016;  
published online 28 November 2016

## References

- Oh, S. H., Legros, M., Kiener, D. & Dehm, G. *In situ* observation of dislocation nucleation and escape in a submicrometre aluminium single crystal. *Nat. Mater.* **8**, 95–100 (2009).
- Zhu, T., Li, J., Samanta, A., Leach, A. & Gall, K. Temperature and strain-rate dependence of surface dislocation nucleation. *Phys. Rev. Lett.* **100**, 025502 (2008).
- Lu, L., Sui, M. L. & Lu, K. Superplastic extensibility of nanocrystalline copper at room temperature. *Science* **287**, 1463–1466 (2000).
- McFadden, S. X., Mishra, R. S., Valiev, R. Z., Zhilyaev, A. P. & Mukherjee, A. K. Low-temperature superplasticity in nanostructured nickel and metal alloys. *Nature* **398**, 684–686 (1999).
- Raj, R. & Ashby, M. F. On grain boundary sliding and diffusional creep. *Metal. Trans.* **2**, 1113–1127 (1971).
- Yamakov, V., Wolf, D., Phillpot, S. R. & Gleiter, H. Grain-boundary diffusion creep in nanocrystalline palladium by molecular-dynamics simulation. *Acta Mater.* **50**, 61–73 (2002).
- Shan, Z. W. *et al.* Grain boundary-mediated plasticity in nanocrystalline nickel. *Science* **305**, 654–657 (2004).
- Guo, W., Wang, Z. & Li, J. Diffusive versus displacive contact plasticity of nanoscale asperities: temperature- and velocity-dependent strongest size. *Nano Lett.* **15**, 6582–6585 (2015).
- Yamakov, V., Wolf, D., Phillpot, S. R., Mukherjee, A. K. & Gleiter, H. Deformation-mechanism map for nanocrystalline metals by molecular-dynamics simulation. *Nat. Mater.* **3**, 43–47 (2004).
- Chokshi, A. H., Rosen, A., Karch, J. & Gleiter, H. On the validity of the Hall–Petch relationship in nanocrystalline materials. *Scr. Metall.* **23**, 1679–1683 (1989).
- Meyers, M. A., Mishra, A. & Benson, D. J. Mechanical properties of nanocrystalline materials. *Prog. Mater. Sci.* **51**, 427–556 (2006).
- Tian, L., Li, J., Sun, J., Ma, E. & Shan, Z. W. Visualizing size-dependent deformation mechanism transition in Sn. *Sci. Rep.* **3**, 2113 (2013).
- Wang, Y. M. & Ma, E. Three strategies to achieve uniform tensile deformation in a nanostructured metal. *Acta Mater.* **52**, 1699–1709 (2004).
- Dao, M., Lu, L., Asaro, R. J., De Hosson, J. T. M. & Ma, E. Toward a quantitative understanding of mechanical behavior of nanocrystalline metals. *Acta Mater.* **55**, 4041–4065 (2007).
- Wei, Q., Cheng, S., Ramesh, K. T. & Ma, E. Effect of nanocrystalline and ultrafine grain sizes on the strain rate sensitivity and activation volume: fcc versus bcc metals. *Mater. Sci. Eng. A* **381**, 71–79 (2004).
- Ma, E. Instabilities and ductility of nanocrystalline and ultrafine-grained metals. *Scr. Mater.* **49**, 663–668 (2003).
- Nieman, G. W., Weertman, J. R. & Siegel, R. W. Mechanical-behavior of nanocrystalline Cu and Pd. *J. Mater. Res.* **6**, 1012–1027 (1991).
- Richter, G. *et al.* Ultrahigh strength single crystalline nanowhiskers grown by physical vapor deposition. *Nano Lett.* **9**, 3048–3052 (2009).
- Uchic, M. D., Dimiduk, D. M., Florando, J. N. & Nix, W. D. Sample dimensions influence strength and crystal plasticity. *Science* **305**, 986–989 (2004).
- Greer, J. R., Oliver, W. C. & Nix, W. D. Size dependence of mechanical properties of gold at the micron scale in the absence of strain gradients. *Acta Mater.* **53**, 1821–1830 (2005).
- Chen, L. Y., He, M. R., Shin, J., Richter, G. & Gianola, D. S. Measuring surface dislocation nucleation in defect-scarce nanostructures. *Nat. Mater.* **14**, 707–713 (2015).

22. Sun, J. *et al.* Liquid-like pseudoelasticity of sub-10-nm crystalline silver particles. *Nat. Mater.* **13**, 1007–1012 (2014).
23. Zhu, Y. *et al.* Size effects on elasticity, yielding, and fracture of silver nanowires: *in situ* experiments. *Phys. Rev. B* **85**, 045443 (2012).
24. Wolf, D., Yamakov, V., Phillpot, S. R., Mukherjee, A. & Gleiter, H. Deformation of nanocrystalline materials by molecular-dynamics simulation: relationship to experiments? *Acta Mater.* **53**, 1–40 (2005).
25. Zheng, H. *et al.* Discrete plasticity in sub-10-nm-sized gold crystals. *Nat. Commun.* **1**, 144 (2010).
26. Li, J. *et al.* Diffusive molecular dynamics and its application to nanoindentation and sintering. *Phys. Rev. B* **84**, 054103 (2011).
27. Mishra, R. S., Valiev, R. Z., McFadden, S. X. & Mukherjee, A. K. Tensile superplasticity in a nanocrystalline nickel aluminide. *Mater. Sci. Eng. A* **252**, 174–178 (1998).
28. Zhong, L., Wang, J. W., Sheng, H. W., Zhang, Z. & Mao, S. X. Formation of monatomic metallic glasses through ultrafast liquid quenching. *Nature* **512**, 177–180 (2014).
29. Wang, J. W. *et al.* *In situ* atomic-scale observation of twinning-dominated deformation in nanoscale body-centred cubic tungsten. *Nat. Mater.* **14**, 594–600 (2015).
30. Wu, Z. X., Zhang, Y. W., Jhon, M. H., Gao, H. J. & Srolovitz, D. J. Nanowire failure: long = brittle and short = ductile. *Nano Lett.* **12**, 910–914 (2012).
31. Rice, J. R. Dislocation nucleation from a crack tip: an analysis based on the Peierls concept. *J. Mech. Phys. Solids* **40**, 239–271 (1992).
32. Kim, S. Y., Lee, I. H. & Jun, S. Transition-pathway models of atomic diffusion on fcc metal surfaces. I. Flat surfaces. *Phys. Rev. B* **76**, 245407 (2007).
33. Kim, S. Y., Lee, I. H. & Jun, S. Transition-pathway models of atomic diffusion on fcc metal surfaces. II. Stepped surfaces. *Phys. Rev. B* **76**, 245408 (2007).
34. Fisher, S. B. On the temperature rise in electron irradiated foils. *Radiat. Eff.* **5**, 239–243 (1970).
35. Ala-Nissila, T., Ferrando, R. & Ying, S. C. Collective and single particle diffusion on surfaces. *Adv. Phys.* **51**, 949–1078 (2002).
36. Greer, J. R. & Nix, W. D. Nanoscale gold pillars strengthened through dislocation starvation. *Phys. Rev. B* **73**, 245410 (2006).
37. Masumura, R. A., Hazzledine, P. M. & Pande, C. S. Yield stress of fine grained materials. *Acta Mater.* **46**, 4527–4534 (1998).
38. Ramachandramoorthy, R., Gao, W., Bernal, R. & Espinosa, H. High strain rate tensile testing of silver nanowires: rate-dependent brittle-to-ductile transition. *Nano Lett.* **16**, 255–263 (2016).
39. Filleter, T. *et al.* Nucleation-controlled distributed plasticity in penta-twinned silver nanowires. *Small* **8**, 2986–2993 (2012).
40. Zheng, H., Wang, J. W., Huang, J. Y., Wang, J. B. & Mao, S. X. Void-assisted plasticity in Ag nanowires with a single twin structure. *Nanoscale* **6**, 9574–9578 (2014).
41. Peng, C., Zhan, Y. J. & Lou, J. Size-dependent fracture mode transition in copper nanowires. *Small* **8**, 1889–1894 (2012).
42. Kiener, D. & Minor, A. M. Source truncation and exhaustion: insights from quantitative *in situ* TEM tensile testing. *Nano Lett.* **11**, 3816–3820 (2011).
43. Shan, Z. W., Mishra, R. K., Asif, S. A. S., Warren, O. L. & Minor, A. M. Mechanical annealing and source-limited deformation in submicrometre-diameter Ni crystals. *Nat. Mater.* **7**, 115–119 (2008).
44. Yu, Q. *et al.* The nanostructured origin of deformation twinning. *Nano Lett.* **12**, 887–892 (2012).
45. Huang, L. *et al.* A new regime for mechanical annealing and strong sample-size strengthening in body centred cubic molybdenum. *Nat. Commun.* **2**, 547 (2011).

## Acknowledgements

S.X.M. acknowledges support from NSF CMMI 1536811 through University of Pittsburgh. This work was performed, in part, at the Center for Integrated Nanotechnologies, an Office of Science User Facility operated for the US Department of Energy (DOE) Office of Science by Los Alamos National Laboratory (Contract DE-AC52-06NA25396) and Sandia National Laboratories (Contract DE-AC04-94AL85000), and at the William R. Wiley Environmental Molecular Sciences Laboratory, a national scientific user facility sponsored by US Department of Energy, Office of Biological and Environmental Research and located at PNNL. PNNL is operated by Battelle for the US Department of Energy under contract DE-AC05-76RLO1830. F.S. acknowledges support from NSF grant No. DMR-1410646 and the computational resources provided by the Extreme Science and Engineering Discovery Environment (XSEDE) supported by NSF grant No. ACI-1053575.

## Author contributions

L.Z. and S.X.M. conceived and designed the experiments. L.Z. and Y.H. conducted the *in situ* TEM experiments under the direction of S.X.M. L.Z. performed the experimental data analysis. F.S. carried out the computer simulations. F.S. and L.Z. developed the kinetic model. All authors contributed to discussion of the results. L.Z., F.S. and S.X.M. wrote the manuscript.

## Additional information

Supplementary information is available in the [online version of the paper](#). Reprints and permissions information is available online at [www.nature.com/reprints](http://www.nature.com/reprints). Correspondence and requests for materials should be addressed to F.S. or S.X.M.

## Competing financial interests

The authors declare no competing financial interests.

## Methods

**In situ tensile testing.** The metals investigated in this work are high-purity (99.999%) Ag and Pt provided by ESPI Metals. The Ag and Pt nano-tips were generated at the fracture edge of bulk metallic substrates<sup>28</sup>. *In situ* tensile tests were conducted with a Nanofactory scanning tunnelling microscope (STM) holder inside an FEI Tecnai F30 TEM. Two sharp nano-tips, or in some cases one tip and one particle deposited on a tungsten probe, with viewing directions along low-index zone axes (for example (110)) were selected to be welded together by applying either an electric pulse<sup>28</sup> or a constant voltage<sup>29</sup>. These procedures generate bridge-shaped single crystals with controllable dimensions that are epitaxially grown from one substrate (for example, the left-side substrate) and connected to either a tungsten probe (Supplementary Fig. 1a) or another substrate (Supplementary Fig. 1b) at the opposite side with one boundary in between (orange dash lines in Supplementary Fig. 1). The middle segment of the single-crystalline nano-bridge has a smaller diameter and higher tensile stress compared to those at either end, and therefore concentrates all plastic deformation (Supplementary Fig. 2), serving as the gauge section, as indicated in Supplementary Fig. 1 and outlined by dotted lines in Fig. 1 as well as Supplementary Figs 2 and 3. Nanostructures for mechanical testing purpose are often fabricated by focused ion beam milling or by attaching NWs to testing devices with focused electron/ion beam assisted Pt deposition, both of which tend to introduce surface contamination layers. The approach in this work produces nanostructures with very clean surfaces, and is therefore ideal for studying surface diffusive plasticity. The strain rate during tensile loading was controlled by how fast the piezo-manipulator of the STM holder was retracted.

**Molecular dynamics simulations.** MD simulations were conducted using the software LAMMPS<sup>46</sup>. Ag and Pt metals were simulated with the embedded-atom-method (EAM) potentials by Wu and Trinkle<sup>47</sup> and Sheng *et al.*<sup>48</sup>, respectively. These potentials have been optimized to predict accurate values for stacking-fault energies in these metals in good agreement with experimental and *ab initio* data. The simulated stable and unstable stacking-fault energies were found to be equal to 18 mJ m<sup>-1</sup> and 115 mJ m<sup>-1</sup>, respectively, for the Ag potential, and 118 mJ m<sup>-1</sup> and 268 mJ m<sup>-1</sup>, respectively, for the Pt potential. Furthermore, Wu and Trinkle's Ag potential<sup>47</sup> has been optimized to accurately simulate surface self-diffusion of adatoms. A circular NW with a double conical shape of length 68.0 nm was modelled with the diameters of the largest and smallest cross-sections equal to 24 nm and 20 nm, respectively. Periodic boundary conditions were imposed along the NW axis, while the sides were kept free in all other directions. The long axis and loading direction were oriented along the [112] direction. The time step was 5 fs. The energy of the models was minimized by the

conjugate-gradient method, then relaxed for 20 ps under zero pressure using an isothermal–isobaric (NPT) ensemble with a Nose–Hoover thermostat at 300 K, 600 K or 900 K  $\pm$  2 K. Following relaxation, pure tensile deformation at the same temperature was carried out by stretching the simulation box along the [112] direction at a constant engineering strain rate in the canonical (NVT) ensemble. Four different strain rates between  $4 \times 10^7$  s<sup>-1</sup> and  $4 \times 10^8$  s<sup>-1</sup> were studied. Due to inherently high strain rates in MD, the extent of surface diffusion was controlled by increasing the temperature from 300 to 900 K for Ag—that is, by augmenting the homologous temperature. We have computed the homologous temperature for 900 K by averaging the melting temperature of  $T_m = 1,267$  K predicted by the EAM interatomic potential<sup>47</sup>, and the experimental value of 1,234 K published by Castro *et al.*<sup>49</sup> for bulk Ag. Castro *et al.*<sup>49</sup> also discussed the melting temperature of Ag nanoparticles, and found an only 4% decrease in melting temperature for a 10-nm-radius Ag cluster compared to bulk Ag, which was considered negligible in this study. For Pt, we considered  $T_m = 1,890$  K obtained with the interatomic potential developed by Sheng *et al.*<sup>48</sup>. Atomic-level snapshots of NW deformation were studied in the atomic visualization software Ovito<sup>50</sup> using the polyhedral template matching analysis, the atomic shear strain calculation and the non-affine squared displacements ( $D_{\min}^2$ ) calculation. The virial theorem and relaxed (undeformed) atomic volume were used to calculate the axial stress in the NWs. The strain was obtained by dividing the box length in the direction of deformation by the initial length. Stress–strain calculations were based on the periodic length and average diameter, and did not take into account the local deformation due to necking. Error in strain calculations was limited because the simulations were performed at a constant engineering strain rate.

## References

46. Plimpton, S. Fast parallel algorithms for short-range molecular-dynamics. *J. Comput. Phys.* **117**, 1–19 (1995).
47. Wu, H. H. & Trinkle, D. R. Cu/Ag EAM potential optimized for heteroepitaxial diffusion from *ab initio* data. *Comput. Mater. Sci.* **47**, 577–583 (2009).
48. Sheng, H. W., Kramer, M. J., Cadien, A., Fujita, T. & Chen, M. W. Highly optimized embedded-atom-method potentials for fourteen fcc metals. *Phys. Rev. B* **83**, 134118 (2011).
49. Castro, T., Reifengerger, R., Choi, E. & Andres, R. P. Size-dependent melting temperature of individual nanometer-sized metallic clusters. *Phys. Rev. B* **42**, 8548–8556 (1990).
50. Stukowski, A. Visualization and analysis of atomistic simulation data with OVITO—the Open Visualization Tool. *Modelling Simul. Mater. Sci. Eng.* **18**, 015012 (2010).